

# Multimodal Data Analytics for Nuclear Facility Monitoring

Christopher Stewart,<sup>1, a)</sup> Bethany L. Goldblum,<sup>1</sup> Shruthi Chockkalingam,<sup>2</sup>  
Suchismita Padhy,<sup>3</sup> Yi-Ting Alicia Tsai,<sup>3</sup> Pedro Vicente Valdez,<sup>1</sup> and Austin  
Wright<sup>2</sup>

<sup>1)</sup>*Department of Nuclear Engineering, University of California, Berkeley CA USA*

<sup>2)</sup>*Department of Electrical Engineering and Computer Sciences, University of California, Berkeley CA USA*

<sup>3)</sup>*School of Information, University of California, Berkeley CA USA*

<sup>a)</sup>*Corresponding author: clstewart@berkeley.edu*

**Abstract.** Recent progress in the development of multisensors has opened opportunities for indirect physical sensing for proliferation detection applications, where numerous data modalities can be measured in real-time—including acceleration, magnetic field, pressure, temperature, humidity, ambient light, and passive IR, among others. Using a wireless multisensor network, data were collected in four experimental campaigns at the 88-Inch Cyclotron at Lawrence Berkeley National Laboratory, which served as a proxy nuclear weapons facility. The cyclotron operational status was classified via supervised learning using a multilayer feed-forward neural network and a suite of sensing modalities as inputs. Using multisensor networks deployed inside the facility, the classifier consistently scored a Matthews Correlation Coefficient (MCC)  $> 0.90$ ; with sensors deployed outside the facility, the MCC dropped to 0.72. As the space of possible measurements in a multisensor network is large (e.g., a network composed of only five nodes generating seven data products per second corresponds to over three million data products per day), techniques for feature engineering for multisensor devices in nonproliferation applications were explored. Permutation importance was used to evaluate the input features according to their contribution to classification success and the classification accuracy as a function of sensor loadout was obtained. This work demonstrates the viability of indirect physical sensing for characterization of nuclear facility operations and provides a quantitative basis for optimized multisensor design for specific deployment scenarios.

## 1. INTRODUCTION

The detection of the development of a nuclear weapons program is hindered by the need to continuously verify the absence of undeclared nuclear materials and weapons-relevant activities. For declared nuclear facilities, unattended remote monitoring has been recognized by the International Atomic Energy Agency as a valuable supplement to onsite inspections for safeguards and verification [1]. In addition to electronic seals and digital cameras, technical near-field approaches to this problem have traditionally relied upon the detection of direct chemical or isotopic signatures of nuclear facility operations [2]. Wireless multisensor networks offer new low-cost opportunities for surveillance and safeguards that enable timely and accurate detection of ambient conditions [3]. This work demonstrates the use of wireless multisensor networks for characterization of nuclear facilities operations using an indirect physical sensing approach.

Indirect sensing, via multisensor data fusion, has the potential to provide an integrated picture of difficult-to-detect phenomena, where composite collateral signals can be used as proliferation indicators. Recent developments in ultra-low-power wireless multisensor networks, in concert with advances in statistical machine learning, offer a path forward for innovation in data analytics for proliferation detection and nuclear material security. In this work, wireless networks of multisensors—termed *canaries*—are used together with supervised learning algorithms to characterize operations at the 88-Inch Cyclotron at Lawrence Berkeley National Laboratory. Canaries, described in Sec. 2, are small enough to be fielded unobtrusively at facilities of interest and have the potential to become a capstone indirect physical sensor platform for proliferation detection and treaty verification.

Experimental inquiry was conducted over four distinct campaigns with varied numbers of nodes and spatial deployments of the wireless multisensor network. Both additive and subtractive algorithms were employed to rank-order the input features based on their permutation importance and quantify their relative contribution to characterizing cyclotron beam status. The experimental methods are described in Sec. 3 along with a data overview. The approach to data analysis including pre-processing methods, the supervised learning model, metrics for classification performance evaluation, and feature engineering techniques are described in Sec. 4. The results of supervised classification approaches to characterization of facility operations for both full and reduced feature sets are provided in Sec. 5. Concluding remarks are given in Sec. 6.

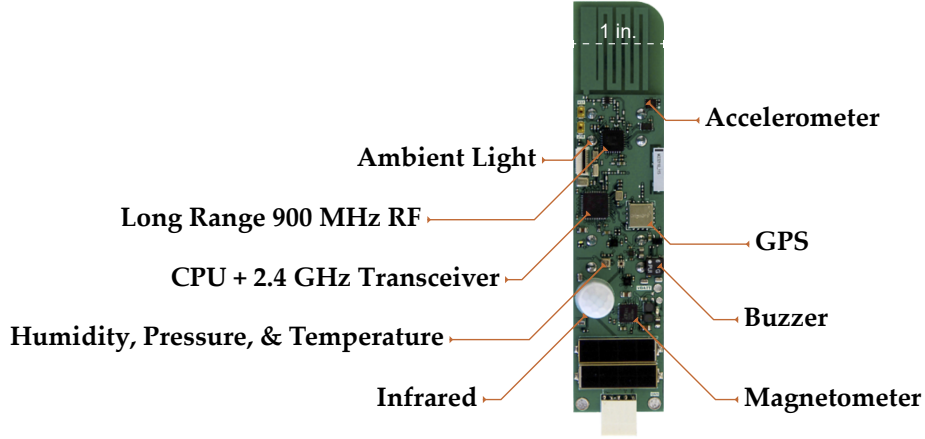


FIGURE 1: Diagram of the canary sensor platform.

TABLE I: Canary sensor specifications.

Modality	Hardware
Light	Texas Instruments OPT3001 [4]
Acceleration	STMicroelectronics LIS2DE12 [5]
Magnetic Field	STMicroelectronics LIS3MDL [6]
Pressure	Bosch Sensortec BME280 [7]
Temperature	Bosch Sensortec BME280 [7]
Humidity	Bosch Sensortec BME280 [7]
Motion	Panasonic EKMB1101111 [8]
Position	OriginGPS ORG4572 [9]

## 2. CANARY: A WIRELESS MULTISENSOR PLATFORM

Each canary in the wireless sensor network is a small, low-power platform for an array of basic physical sensors. The canary is capable of measuring up to 12 data products from 8 different sensing modalities using commercial off-the-shelf sensors. Sensing modalities currently enabled on the device include light, acceleration (3-axis), magnetic field (3-axis), pressure, temperature, humidity, motion, and position. An image of the canary device is shown in Fig. 1, and sensor details are provided in Table I. The onboard central processing unit is an ultra-low-power wireless microcontroller unit, Texas Instruments CC2650, with a 32-bit Arm Cortex-M3 processor with a clock speed up to 48 MHz and 128 kB of in-system programmable flash memory. The CC2650 device features a 2.4 GHz RF transceiver compatible with IEEE 802.15.4, which governs the low-rate personal area network.

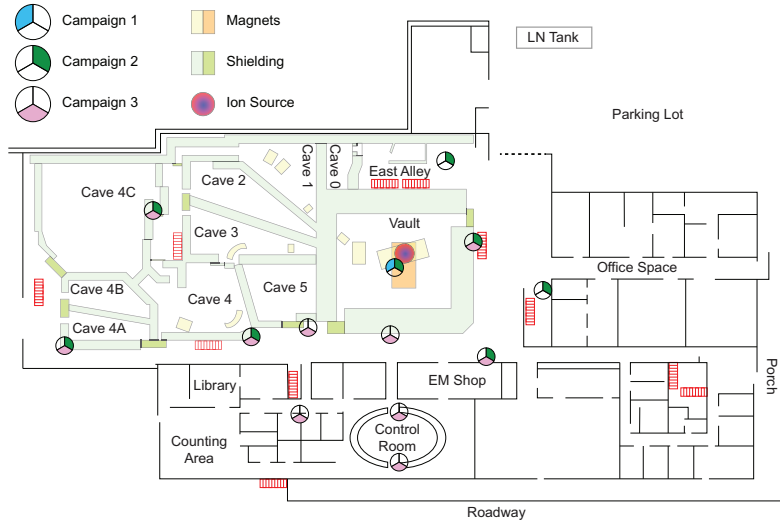
Canary machine-to-machine communication was accomplished using 6LoWPAN, a low power consumption technology for wireless data exchange over short range [10]. Each canary was configured using the Contiki operating system designed for low-power microcontrollers [11]. All nodes were configured as 6LoWPAN routers and dynamically self-assemble into a mesh/tree network that enables message propagation via node-to-node hopping. Sensor polling rates and data exchange intervals are adjustable based on the Texas Instruments CC2650 real time clock using a Unix Epoch time configuration; these were set on a per-campaign basis to maximize network uptime. The Texas Instruments CC2531 USB dongle configured with a Contiki Slip radio was plugged into a portable Linux host, a personal computer running Ubuntu 16.04.2 LTS. The wireless sensor 6LoWPAN network was connected to the IP-based network using the CETIC 6LBR border router platform. Mosquitto was used to implement the Message Queuing Telemetry Transport (MQTT) publish-subscribe messaging protocol on the Linux host [12]. The collected data were logged in real-time using a MariaDB relational database [13].

### 3. EXPERIMENTAL METHODS AND DATA OVERVIEW

The canaries were deployed in four experimental campaigns conducted at the 88-Inch Cyclotron at Lawrence Berkeley National Laboratory. In this work, the cyclotron is representative of an isotope-production facility in a nuclear proliferation pathway [14]. Charged particles are accelerated in a spiral to high energies in the cyclotron using an electric field switched at radio frequencies while constrained to a particular path using powerful magnets. The particles are extracted at the edge of the main magnets and then guided in a beam via a series of switching and bending magnets to downstream experimental end stations occupying well-shielded caves where various low-energy nuclear physics experiments are performed [15]. The entire cyclotron is enclosed in a shielding superstructure consisting of large cement blocks.

The VENUS ion source at the LBNL 88-inch Cyclotron employs a 4 T magnetic field at injection, which remains measurable despite the shielding yoke in place to reduce the stray field profile [16]. The cyclotron acceleration chamber is maintained at ultra-low vacuum ( $\sim 100 \mu\text{Pa}$ ) by several diffusion and cryogenic pumps [17, 18]. These systems can cause a slight pressure differential with the surrounding atmosphere that may be detectable by the canary pressure sensors. During operation, the cyclotron also dissipates large amounts of heat. Some of the largest heat sources are the main magnets and the RF field magnets, which draw an average of 1.3 MW of power. The cooling systems for the cyclotron equipment incorporate a large centrifugal pump to dissipate up to 2 MW in addition to auxiliary systems consisting of dedicated pumps and compressors which produce low-frequency vibrations [18]. High temperature sources such as those found in the VENUS ion source ovens [16] can cause local temperature and humidity differentials which may be measurable using the canary sensors. The light and motion sensors on the canary are helpful to capture the differences in pattern-of-life phenomena in the facility between operational states.

#### 3.1. Data Collection Campaigns



(a) Deployment map for the three indoor experimental campaigns. The canary placement is indicated by the tricolored circle icons.



(b) Overhead image of Building 88, which houses the cyclotron. In this outdoor experimental campaign, canary placement is indicated by the gold circles.

FIGURE 2: Experimental setup at the 88-Inch Cyclotron at Lawrence Berkeley National Laboratory.

The canaries in each experimental campaign were deployed to static locations and only disturbed when replacing their batteries. Each indoor campaign was carried out with a different objective (i.e., proof-of-concept, physical conditions monitoring, and pattern-of-life analysis). The map of the three indoor deployments is shown in Figure 2a. The fourth campaign, an outdoor deployment depicted in Figure 2b, explored the degree to which data obtained outside the building could be used to predict operations conducted inside the facility. For all campaigns, the cyclotron operational status (on/off) was also recorded using ground truth obtained from operator logs, which included the main magnet status (on/off) and the RF field status (on/off). The cyclotron was considered “on” if both the main magnet and RF fields were active.

TABLE II: Summary of settings for the four experiments. The fifth column indicates the class prevalence of samples in each campaign, corresponding to cyclotron operational status.

Campaign	Canaries (No.)	Polling Frequency (Hz)	Samples (No.)	On/Off (%)
1	3	1.0	108,385	88.9/11.1
2	14	0.07	615,122	37.8/62.2
3	10	0.05	75,350	80.9/19.1
4	15	0.05	473,627	69.6/30.4

The first campaign—a proof of concept—consisted of only three devices and assessed whether canary-based indirect physical sensing could provide meaningful data in the characterization of nuclear facilities operations. For this reason, all canaries in the network were placed atop the shielding structure housing the cyclotron’s primary magnets. This location was also very close ( $\sim 1.2$  m) to the cyclotron’s primary ion source. Data were collected for 72 hours.

The wireless sensor network topology in the second campaign was constructed to enable detection of a wide range of physical phenomena at the facility, including emanations from the ion source, magnets, RF, and vacuum and cooling systems. The spatial arrangement of the network encompassed the entire high bay which houses the cyclotron-shielding superstructure. Seven pairs of canaries, for a total of 14, were placed atop and around the shielding to provide redundant coverage. The canary positions ranged from several to almost 30 m from the main magnets. One of the peripheral pairs of canaries had to be relocated mid-campaign to accommodate facility maintenance efforts. Data were taken for 16 days.

The third deployment further extended the spatial coverage of the sensor network to include some personnel areas (i.e., control room, employee cubicles) while maintaining most of the deployment locations in the second campaign as non-redundant nodes. In this campaign, the shortest canary-to-main-magnet standoff distance was approximately 9 m. The expansion to personnel areas offers the potential for new classification pathways based on pattern-of-life analysis. In addition to the movement of the collection points to the periphery of the main magnet, this campaign also served to provide testing data for situations in which network connectivity was intermittent. Data for this campaign were collected for 15 days.

The fourth campaign included fifteen canaries, all of which were deployed outside the cyclotron facility to gain insight on the degree to which outdoor surveillance can reveal indoor facility operations. The bulk of the network was located on or around the front porch of the building and spread around the building’s southeast corner, with the most distal canaries perched across a small parking lot. The collection point was located in the lobby against an exterior-facing window, giving it line-of-sight to two canaries. To protect the boards from the elements, each was enclosed within a plastic bag. The bags were anchored using sufficient ballast to prevent displacement by winds. Data were collected for approximately one month.

### 3.2. Data Overview

The sizes of the datasets generated during each campaign and the prevalence of each label class for their samples are summarized in Table II. The distributions of physical signatures for Campaign 2 are shown in Figure 3, which illustrates the lack of clear separation in the sensor data between the “beam on” and “beam off” facility states. The data from the other acquisition campaigns displayed a similarly high degree of overlap for the facility operation states. A small fraction of the values for each modality differ significantly from the bulk of the data; these plots are truncated to provide a more clear view of the distributions.

## 4. ANALYSIS TOOLS & ALGORITHMS

### 4.1. Preprocessing

Following the experiments, canary data were labeled as to the cyclotron operational status (i.e., two classes: “beam on” or “beam off”). During preprocessing, the data from each canary were treated on a per-device basis. Data cleaning was accomplished by removing all events that exhibited accelerometer values at least three mean absolute deviations (MADs)

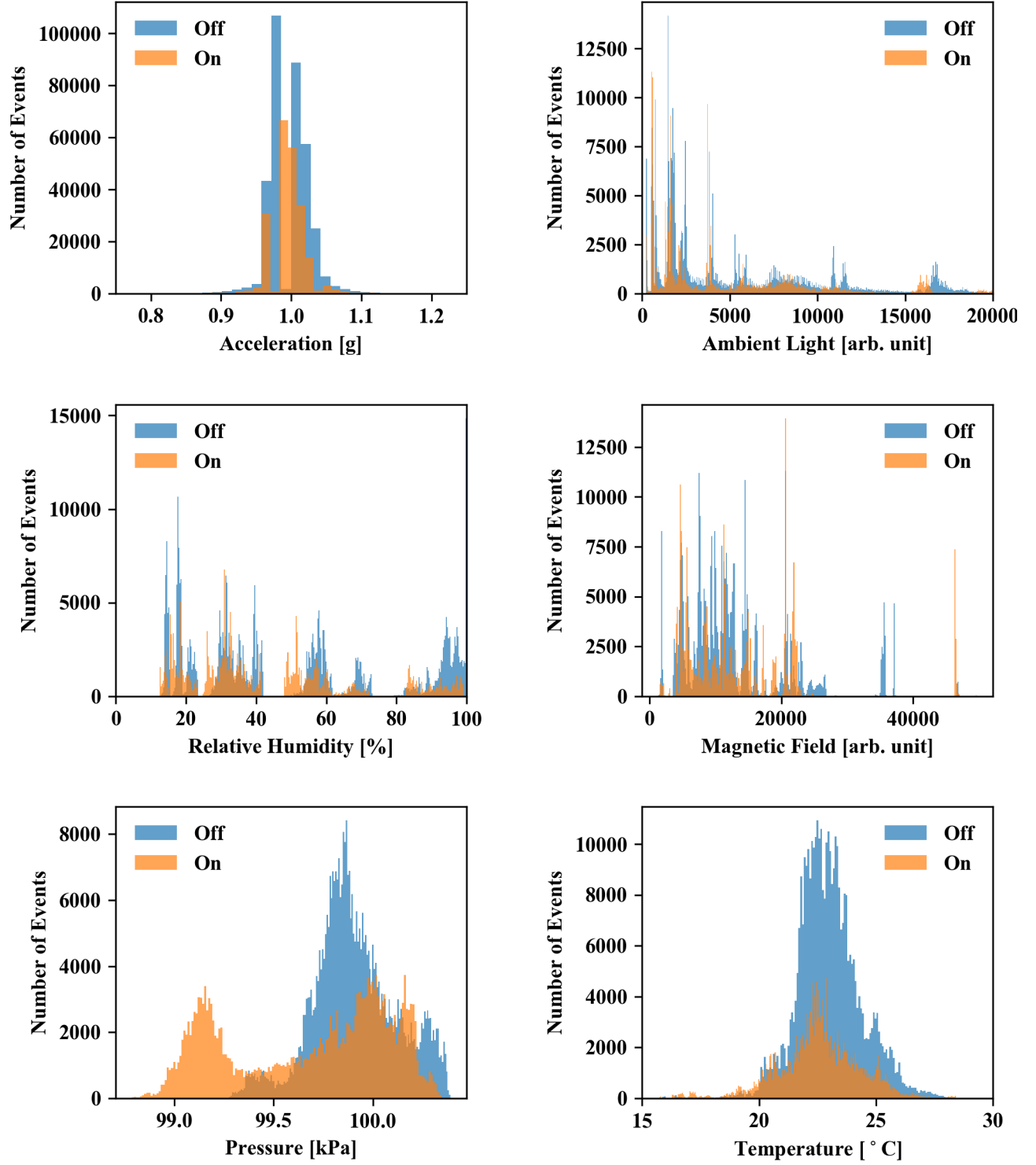


FIGURE 3: Distributions of the sensor data collected by all canaries in Campaign 2 for six sensing modalities. The blue and gold distributions correspond to events obtained during “beam off” and “beam on” states, respectively.

outside their mean values. The MAD is given by:

$$\text{MAD} = \frac{1}{n} \sum_{i=1}^n |x_i - \mu|, \quad (1)$$

where  $\mu$  is the mean of all the values for a given sensing modality,  $x_i$  is each individual data product, and  $n$  is the total number of data products. The MAD was favored over the traditional standard deviation as extreme outliers in the latter (which are not representative of the data set as a whole) would contribute more to the measure of variability. Such large outliers should, in the case of static locations, only be the result of perturbations of the experimental setup from direct human interactions, e.g., changing the canary's batteries or power-cycling the board. An algorithmic approach was taken to cleaning rather than manually removing data corresponding with logged experimenter perturbations of the network to account for potential undocumented interference from the cyclotron staff. Such an approach may also be implemented in real-world deployment scenarios due to human or wildlife interference.

Data inspection revealed a strong correlation between the temperature, humidity, and pressure data measured by the canaries and atmospheric conditions measured at nearby weather stations. To isolate temperature, humidity, and pressure conditions reflective of cyclotron operations, the canary values from these modalities were calibrated by subtracting the linearly-interpolated mean hourly data gathered from a National Oceanic and Atmospheric Administration (NOAA) station at the Oakland International Airport located 24.1 km from the 88-Inch Cyclotron [19]. For the NOAA pressure data, altitude correction was performed using the barometric formula prior to subtraction [20]. After cleaning and calibration, the data were standardized on a per-device basis to have a mean of zero and unit variance.

For each individual modality, data from all canaries were aggregated prior to ingestion in the supervised classification algorithm to focus on the utility of multisource data fusion as opposed to the spatial geometry of the network—though methods that also take into account sensor network topology are emerging [21, 22, 23]. Aggregating the data from multiple canaries removes the ability to discern patterns-of-life signatures local to a single canary (global patterns-of-life signals are unaffected), but obviates the need for global knowledge of the wireless sensor network topology, which could be important for surveillance systems deployed in real-world scenarios. To preserve a test set for final model evaluation, 30% of each dataset was sequestered; the remaining data were split into training (50%) and validation (20%) sets for hyperparameter optimization. Given the imbalanced class distributions, particularly for Campaigns 1 and 3 (see Table II), stratified sampling was employed to ensure class balance in the training, validation, and test sets.

## 4.2. Classifier

A multilayer feed-forward neural network was chosen as the classifier in a supervised learning approach. Multilayer neural networks trained on labeled data have demonstrated excellent classification accuracy, while not incurring the larger computation costs associated with deeper network architectures [24]. A feed-forward neural network is a directed computational graph of nodes arranged into layers; at each layer, values from the incoming edges are weighted, summed, and biased before being passed into an activation function whose output value is passed to nodes in the next layer. While a feed-forward network can approximate an arbitrary function with one hidden layer consisting of a large number of nodes, adding a second hidden layer allows for the introduction of substantial nonlinearities by nesting activation functions to achieve a given approximation fidelity with a smaller total number of hidden nodes than in a single layer. Additional hidden layers have been shown to improve classification performance in some applications (e.g., image classification), but each additional layer introduces additional model parameters which require a correspondingly-larger training set and increased computation time. A dropout layer, which removes a fraction of randomly-selected nodes in each layer during each training epoch, was added prior to each non-input layer to combat overfitting [25]; during prediction dropout layers are inactive.

The number and size of the hidden layers were constrained by the size of the training set from the acquisition campaign with the least data. The absolute limit on the number of free parameters in the model is the number of samples in the training set. However, for each parameter to be meaningfully adjusted across each epoch of the iterative training process, their multiplicity should be much less than the size of the training set:

$$\sum_{l=2}^L n_l n_{l-1} + n_l \ll n_{\text{samples}}, \quad (2)$$

where  $n_l$  is the number of nodes in layer  $l$  with  $l = 1$  denoting the input layer,  $L$  is the total number of layers, and  $n_{\text{samples}}$  is the number of samples in the training set. The left-hand side of the inequality represents the total number of free

parameters in the network. The number of connections for a dense layer in a feed-forward neural network is the number of nodes in layer  $l$  multiplied by the number of nodes in layer  $l - 1$ , since each node is fully connected to every node in the previous layer. There is also a bias applied to the weighted sum of the previous layer's outputs arriving at each node, which provides an additional  $n_l$  parameters. Accounting for dropout, the parameter multiplicity in this work was kept at least an order of magnitude lower than the number of samples in the training set. The maximum size of the hidden layers according to this constraint was 25 nodes per layer. The number of nodes up to this limit was regularly sampled for the first layer size during hyperparameter optimization, and the second layer was constrained to be no larger than the size of the first.

The exponential linear unit was chosen as the activation function for the internal nodes because it avoids the vanishing gradient and dead neuron problems while providing quick convergence in comparison studies [26]. A softmax activation function was used in the output layer to normalize unbounded real numbers into a probability distribution across the available classes. The hyperparameter search space, described in Table III, was grid-searched and the optimal values corresponding to each campaign were used in the full-feature and feature-selection algorithms. Each model was trained until either 1000 epochs of the training dataset had occurred or no significant improvement in predictions made on the validation set had been achieved for 25 epochs.

TABLE III: Hyperparameter search space for the neural network classifier.

Hyperparameter	Value(s)
Activation Function (Hidden Layers)	Exponential Linear Unit
Activation Function (Output Layer)	Softmax
Batch Size	1024 samples
Dropout Rate	{0.00, 0.05, 0.10, 0.15, 0.20, 0.25}
Hidden Layer Nodes (Layer 1, Layer 2)	{(5, 5), (10, 5), (10, 10), (15, 5), (15, 10), (15, 15), (20, 5), (20, 10), (20, 15), (20, 20), (25, 5), (25, 10), (25, 15), (25, 20), (25, 25)}
Learning Rate	$\{1, 2, 5\} \times 10^{\{-1, -2, -3, -4\}}$
Optimizer	Adam: $\beta_1 = 0.9$ , $\beta_2 = 0.999$ [27]
Loss Function	Categorical Cross-Entropy

### 4.3. Evaluation Metrics

In nuclear proliferation detection, the absence of some derived signals is as important to identify as their presence. An accuracy metric for performance evaluation in statistical machine learning provides the fraction of correct classifications, but fails to properly characterize performance in classification problems with class imbalance. The Matthews Correlation Coefficient (MCC) was adopted in this work as it is useful in the presence of high disparity in class prevalence and penalizes misclassifications of both types [28, 29]. The two-class MCC is calculated as follows:

$$\text{MCC} = \frac{(TP \times TN) - (FP \times FN)}{\sqrt{(TP + FP)(TP + FN)(TN + FP)(TN + FN)}}, \quad (3)$$

where  $TP$  is the number of true positives,  $FP$  is the number of false positives,  $TN$  is the number of true negatives, and  $FN$  is the number of false negatives in the test set predictions. An MCC of 1 indicates perfect performance, a value of -1 (in the two-class case) results from exactly incorrect predictions, and a value of 0 corresponds to the classifier providing no improvement over randomly sampling the distribution of the class prevalences. If the classifier either makes no predictions in one of the classes or one of the classes is entirely absent from the test set, the denominator will be zero; in this case, the denominator is set to 1. This results in  $\text{MCC} = 0$ , which is equivalent to the outcome of no information gained from implementing the model.

### 4.4. Feature Engineering

The permutation importance was used to evaluate the contribution of each sensing modality to the optimized models' classification performance. Permutation importance is a model-agnostic measure that has been shown to be unbiased for

non-linear classifiers [30]. One by one, the values of each input feature are randomly permuted (leaving the other input features in their original state), and the modified inputs are used to classify the test data. The relative decrease of the test set prediction score with the input values of a given permuted feature is the importance of that feature in the full model.

### ***Recursive Feature Elimination***

While the value of each input feature to the full model is useful in assessing already-built sensor packages, the marginal value of each sensing modality is of interest in the design process—especially for arrays of low-cost sensor platforms which are amenable to an iterative development approach and may have deployment-specific differences in full-model feature importance. Also of relevance is the prospect of having one or more sensing modalities scrambled, spoofed, or otherwise confounded during surveillance and monitoring. Using the permutation importance as the basis for evaluation of the impact of lost sensory input on classification performance, the least important feature in the set of inputs to the full model was eliminated. After elimination, a model with identical internal architecture was trained using the reduced input feature set; the permutation importance of this subset of input features was then re-evaluated for the reduced-input model. This process—known as recursive feature elimination (RFE)—was repeated to yield a ranking of all of the sensors [31]. The reduction in the MCC between the models is the marginal value of the sensor to the overall multisensor package.

### ***Recursive Feature Addition***

A forward method of calculating the marginal value of each sensor—recursive feature addition (RFA)—was also implemented to mimic the *ab initio* multisensor research and development process [32]. Instead of recursively eliminating features from an optimized full model, models were trained with identical internal architecture to the full model with each of the individual sensing modalities acting as the only input feature. The modality that most improved the MCC was selected for permanent inclusion. Models were then trained with two input features—the permanently-included feature and one feature from the remaining input set—and the input which provided the greatest improvement in the MCC over the single-input model was permanently added. Recursive implementation of this process adds an additional measure of the marginal value of each sensor to classification performance, which can be used to compare against the RFE approach.

## **5. RESULTS**

The optimized hyperparameter set for each of the campaigns and the classification performance using the full set of input features is shown in Table IV. The optimal dropout rate for all campaigns was 0.0, indicating that the feature space partitioning learned on the training sets via updating the full set of model parameters every epoch generalized well to the respective validation sets. Accuracy is reported alongside the MCC to provide a comparative metric, but the MCC is recommended for performance evaluation due to class imbalance. The optimized classifiers provided substantial improvement above chance for all of the four experimental campaigns. In Campaign 2 in particular, the distributed signal collection and high sensor uptime yielded a prediction of beam status tens of percent above the prevalence of the dominant class.

TABLE IV: Optimal hyperparameters and classification performance of the optimized model for each experimental campaign using the full feature set.

Campaign	Network Architecture	Learning Rate	Class Prevalence (ON/OFF)	Accuracy	MCC
1	(25, 20)	$5 \times 10^{-2}$	88.9/11.1	99.4%	0.970
2	(25, 25)	$2 \times 10^{-2}$	37.8/62.2	96.3%	0.922
3	(20, 20)	$2 \times 10^{-3}$	80.9/19.1	99.2%	0.973
4	(25, 25)	$2 \times 10^{-2}$	69.6/30.4	88.9%	0.732

The feature importance of the sensing modalities obtained using RFE and RFA is shown in Fig. 4a and Fig. 4b, respectively; both are ordered most- to least-important from left to right. Using RFA, the magnetic field was shown to be



the most important feature in all campaigns, which is reasonable given the high magnetic fields present during cyclotron operations. The feature importance determined using RFE also revealed the magnetic field as the most important feature for Campaigns 2 and 4, datasets with low sensor downtime and a relatively large number of samples. For Campaigns 1 and 3, the short data collection period and intermittent network connectivity, respectively, yielded fewer samples in the data sets. This, along with the relatively high class imbalance, may have contributed to spurious correlations. For Campaign 1, which also had low spatial coverage, the last remaining feature provided no classification improvement over the class prevalence distribution resulting in a  $MCC = 0$ . The model trained with humidity as the only input feature got stuck in a local minimum during training in which it always predicted a “beam on” status. This scenario highlights the relative robustness of the RFA algorithm in the case of correlated input features. For all campaigns, both approaches to the determination of feature importance showed a saturation in the MCC with approximately four sensing modalities. This result showcases the importance of multisensor data fusion in proliferation detection, where multiple low-resolution sensing modalities *considered in concert* provide a meaningful assessment relevant for the national security enterprise.

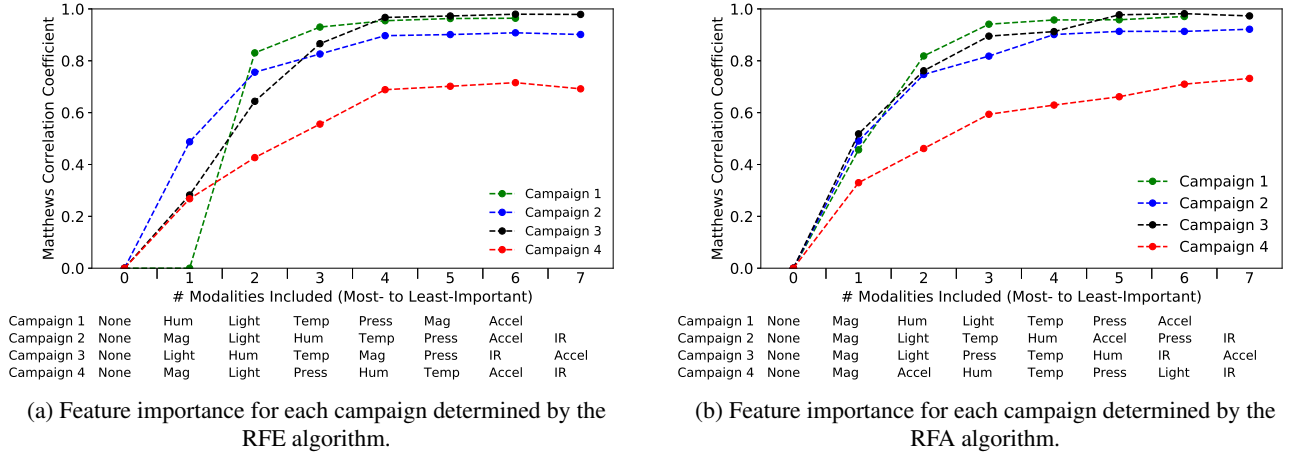


FIGURE 4: The MCC as a function of sensing modality obtained via permutation importance, where the specific feature corresponding to a given MCC for each campaign is denoted below the plot.

## 6. SUMMARY

A network of wireless multisensors was used to evaluate nuclear facility operations at the 88-Inch Cyclotron at LBNL. Four experiments were conducted, each with different deployment configurations, including an outdoor campaign to assess feasibility for anti-access scenarios. Data analysis was performed using supervised classification, and a feed-forward neural network was shown to provide superior classification performance using data gathered within the facility. The minimum sets of data products required for specific detection priorities were explored, with the aim of culling redundant or irrelevant data for a particular assessment. The results of supervised classification using reduced feature sets suggest that similar classification performance can be obtained using these models with only four sensing modalities if facility access is available, which has economic implications for multisensor design and development. In anti-access scenarios, classification performance may be further improved by employing alternate multisensor network topologies and via the use of recurrent neural network models, but additional research is needed. This work demonstrates the use of indirect physical sensing for nonproliferation applications and paves the way for the implementation and deployment of multisensor networks for the detection and monitoring of nuclear facility operations.

## ACKNOWLEDGMENTS

The authors gratefully acknowledge the visionary guidance of H. Kornell and support from the Nevada National Security Site Interdependent Networks team. The technical assistance of Lakshmi Ramesh, Yara Mubarak, and Jared Zhao is also much appreciated. This material is based upon work supported by the Department of Energy National Nuclear Security

Administration by Lawrence Berkeley National Laboratory under Contract DE-AC02-05CH11231, through the Office of Defense Nuclear Nonproliferation Research and Development (DNN R&D) under Award No. 1770585, and through the Nuclear Science and Security Consortium under Award Number DE-NA0003180. This report was prepared as an account of work sponsored by an agency of the United States Government. The views and opinions of authors expressed herein do not necessarily state or reflect those of the United States Government or any agency thereof.

## REFERENCES

1. K. E. Sanders, Y. Y. Liu, and J. M. Shuler, in *Proceedings of the 56th Annual Meeting of the Institute of Nuclear Materials Management* (INMM, Indian Wells, CA USA, 2015).
2. R. S. Kemp, *Annual Review of Earth and Planetary Sciences* **44**, 17 (2016).
3. I. Akyildiz, W. Su, Y. Sankarasubramaniam, and E. Cayirci, *Computer Networks* **38**, 393 (2002).
4. Texas Instruments, “OPT3001: Digital Ambient Light Sensor (ALS) With High-Precision Human-Eye Response,” (2018).
5. STMicroelectronics, “LIS2DE12: 3-axis MEMS accelerometer,” (2018).
6. STMicroelectronics, “LIS3MDL: 3-axis MEMS magnetic field sensor,” (2018).
7. Bosch Sensortec, “BME280: Integrated Environmental Units,” (2018).
8. Panasonic, “EKMB110111,” (2018).
9. OriginGPS, “Spider Series ORG4572,” (2018).
10. A. A. Hasbollah, S. H. S. Ariffin, and M. I. A. Hamini, in *TENCON 2009 - 2009 IEEE Region 10 Conference* (2009) pp. 1–5.
11. A. Dunkels, B. Gronvall, and T. Voigt, in *Proceedings of the 29th Annual IEEE International Conference on Local Computer Networks*, LCN '04 (IEEE Computer Society, Washington, DC, USA, 2004) pp. 455–462.
12. Eclipse Mosquitto, “Eclipse Mosquitto™: An open source MQTT broker,” (2018).
13. MariaDB Foundation, “The MariaDB Foundation—Supporting continuity and open collaboration in the MariaDB ecosystem,” (2018).
14. R. S. Kemp, *Science & Global Security* **13**, 183 (2005).
15. M. K. Covo, R. A. Albright, B. F. Ninemire, M. B. Johnson, A. Hodgkinson, T. Loew, J. Y. Benitez, D. S. Todd, D. Z. Xie, T. Perry, L. Phair, L. A. Bernstein, J. Bevins, J. A. Brown, B. L. Goldblum, M. Harasty, K. P. Harrig, T. A. Laplace, E. F. Matthews, A. Bushmaker, D. Walker, V. Oklejas, A. R. Hopkins, D. L. Bleuel, J. Chen, and S. B. Cronin, *Measurement* **127**, 580 (2018).
16. J. Y. Benitez, K. Y. Franzen, A. Hodgkinson, T. Loew, C. M. Lyneis, L. Phair, J. Saba, M. Strohmeier, and O. Tarvainen, *Review of Scientific Instruments* **83**, 02A311 (2012).
17. Z. Xie, C. Lyneis, D. Clark, A. Guy, and S. Lundgren, *Vacuum improvements for ultra high charge state ion acceleration*, Tech. Rep. (Lawrence Berkeley National Laboratory, Nuclear Science Division, Berkeley, CA, 1998).
18. B. F. Ninemire, Private communication (2019).
19. National Oceanic and Atmospheric Administration, National Centers for Environmental Education, “Climate Data Online,” <https://www.ncdc.noaa.gov/cdo-web/> (2017).
20. M. N. Berberan-Santos, E. N. Bodunov, and L. Pogliani, *American Journal of Physics* **65**, 404 (1997).
21. P. Veličković, G. Cucurull, A. Casanova, A. Romero, P. Liò, and Y. Bengio, arXiv e-prints , arXiv:1710.10903 (2017), arXiv:1710.10903 [stat.ML].
22. A. Jean-Pierre Tixier, G. Nikolentzos, P. Meladianos, and M. Vazirgiannis, arXiv e-prints , arXiv:1708.02218 (2017), arXiv:1708.02218 [cs.CV].
23. R. A. Rossi, R. Zhou, and N. K. Ahmed, arXiv e-prints , arXiv:1704.08829 (2017), arXiv:1704.08829 [stat.ML].
24. Jürgen Schmidhuber, *Neural Networks* **61**, 85 (2015).
25. N. Srivastava, G. Hinton, A. Krizhevsky, I. Sutskever, and R. Salakhutdinov, *The Journal of Machine Learning Research* **15**, 1929 (2014).
26. D.-A. Clevert, T. Unterthiner, and S. Hochreiter, arXiv e-prints , arXiv:1511.07289 (2015), arXiv:1511.07289 [cs.LG].
27. D. P. Kingma and J. Ba, arXiv e-prints , arXiv:1412.6980 (2014), arXiv:1412.6980 [cs.LG].
28. B. Matthews, *Biochimica et Biophysica Acta (BBA) - Protein Structure* **405**, 442 (1975).
29. S. Boughorbel, F. Jarray, and M. El-Anbari, *PLOS ONE* **12**, 1 (2017).
30. A. Altmann, L. Toloşi, O. Sander, and T. Lengauer, *Bioinformatics* **26**, 1340 (2010).
31. I. Guyon, J. Weston, S. Barnhill, and V. Vapnik, *Machine Learning* **46**, 389 (2002).
32. T. Hamed, *Recursive Feature Addition: a Novel Feature Selection Technique, Including a Proof of Concept in Network Security*, Doctoral dissertation, The University of Guelph (2017).